Nanoscale

PAPER

View Article Online
View Journal | View Issue

Open Access Article. Published on 25 February 2016. Downloaded on 1/18/2026 1:16:03 PM.
This article is licensed under a Creative Commons Attribution 3.0 Unported Licence.

Cite this: *Nanoscale*, 2016, **8**, 6721

Organic solar cells with graded absorber layers processed from nanoparticle dispersions

Stefan Gärtner,†[a] Stefan Reich,†[a] Michael Bruns,[b] Jens Czolk[a] and Alexander Colsmann*[a]

Received 5th January 2016,
Accepted 24th February 2016

DOI: 10.1039/c6nr00080k

www.rsc.org/nanoscale

The fabrication of organic solar cells with advanced multi-layer architectures from solution is often limited by the choice of solvents since most organic semiconductors dissolve in the same aromatic agents. In this work, we investigate multi-pass deposition of organic semiconductors from eco-friendly ethanol dispersion. Once applied, the nanoparticles are insoluble in the deposition agent, allowing for the application of further nanoparticulate layers and hence for building poly(3-hexylthiophene-2,5-diyl): indene-C_{60} bisadduct absorber layers with vertically graded polymer and conversely graded fullerene concentration. Upon thermal annealing, we observe some degrees of polymer/fullerene interdiffusion by means of X-ray photoelectron spectroscopy and Kelvin probe force microscopy. Replacing the common bulk-heterojunction by such a graded photo-active layer yields an enhanced fill factor of the solar cell due to an improved charge carrier extraction, and consequently an overall power conversion efficiency beyond 4%. Wet processing of such advanced device architectures paves the way for a versatile, eco-friendly and industrially feasible future fabrication of organic solar cells with advanced multi-layer architectures.

Introduction

As the field progresses and organic photovoltaics advance towards market-readiness, the deposition of functional layers by industrial printing or coating techniques comes into play.[1,2] Pivotal to the transfer strategy from lab to fab is the replacement of the commonly used toxic or chlorinated lab-solvents with eco-compatible agents.[3–7] The quest for eco-compatible solvents turned out to be very challenging since many organic materials do not dissolve in non-chlorinated aromatic hydrocarbons or exhibit very different processing properties. A promising approach to circumvent all issues arising from the deposition of organic bulk-heterojunctions (BHJs) from toxic solvents is the use of organic nanoparticle dispersions in water or alcohol.[8–10] Two synthetic routes to organic nanoparticles have been discussed in the literature: utilizing surfactants, organic nanoparticles can be synthesized in miniemulsions.[11] However, organic solar cells deposited from these aqueous dispersions do not yield high power conversion efficiencies (PCEs), which may be attributed to the surfactants remaining within the active layer where they hamper the photovoltaic performance. Alternatively, nanoparticles from poly(3-hexylthiophene-2,5-diyl) (P3HT) and indene-C_{60} bisadduct (ICBA) can be precipitated in alcohol omitting any surfactants, thereby enabling organic solar cells with PCEs of 4%, almost matching the performance of organic solar cells deposited from chlorinated solvents.[12,13]

In this work, we demonstrate that, besides eco-friendly processing, future device fabrication may benefit from another unique feature of polymer:fullerene nanoparticles: layers that have been applied from nanoparticle dispersions are insoluble in the deposition agent, enabling the sequential deposition of the same material from the same agent and hence the fabrication of advanced multi-layer device architectures. It is known from vacuum processed devices that graded absorber layers, *i.e.*, an increase of the donor concentration in BHJs towards the anode and an increase of the acceptor concentration towards the cathode, lead to enhanced charge carrier transport to the electrodes and hence improved solar cell performance.[14,15] With multi-layer deposition from solution being very challenging, lamination processes were reported as work-around for the fabrication of graded absorber layers.[16]

In this work, we exploit the unique processing properties of organic nanoparticle dispersions towards stepwise wet processing of graded BHJs without relying on complex lamination processes or hardly controllable vertical phase separation in photo-active layers deposited from blend solutions.[17]

[a]*Light Technology Institute, Karlsruhe Institute of Technology (KIT), Engesserstrasse 13, 76131 Karlsruhe, Germany. E-mail: alexander.colsmann@kit.edu*
[b]*Institute of Applied Materials and Karlsruhe Nano Micro Facility, Karlsruhe Institute of Technology (KIT), Hermann-von-Helmholtz-Platz 1, 76344 Karlsruhe, Germany*
† These authors contributed equally to this work.

Open Access Article. Published on 25 February 2016. Downloaded on 1/18/2026 1:16:03 PM.
This article is licensed under a Creative Commons Attribution 3.0 Unported Licence.

Results and discussion

Device architectures

All solar cells were fabricated according to the device architectures A–C that are depicted in Fig. 1. The samples were thermally annealed at 150 °C for 10 min after photo-active layer deposition in order to establish close contact of the nanoparticles and hence to improve charge carrier extraction as reported in the literature before.[12]

Configuration A is a reference solar cell with an inverted device architecture that comprises an indium tin oxide/zinc oxide (ITO/ZnO) bottom cathode, a nanoparticulate P3HT:ICBA BHJ photo-active layer that was deposited from ethanol (EtOH) dispersion, and a poly(3,4-ethylenedioxythiophene):poly(styrenesulfonate)/silver (PEDOT:PSS/Ag) top anode. By applying P3HT on top of the nanoparticulate P3HT:ICBA layer in configuration B, again from dispersion in the non-solvent EtOH, thereby avoiding dissolution of the P3HT:ICBA layer below, we changed the vertical distribution of different nanoparticles throughout the layer leading to a grading of the polymer:fullerene concentration. In configuration C, we additionally deposited an ICBA layer under the nanoparticulate P3HT:ICBA layer in order to introduce another grading step. Since ICBA alone does not form stable nanoparticles in the precipitation process, we deliberately deposited the ICBA layer from *o*-dichlorobenzene solution. To ensure better comparability of the devices, the layer thicknesses in all configurations were chosen to maintain the absorption strength by using the same amount (mass) of photo-active P3HT, neglecting fullerene absorption and thin-film interference. Due to the fullerene deficiency in the neat P3HT nanoparticles, the combined thickness of the P3HT:ICBA/P3HT nanoparticulate layer is lower in configuration B (h = 174 nm) than in the reference configuration A (h = 196 nm). In configuration C, the thickness of the neat ICBA layer was chosen to compensate for the fullerene deficiency in the neat P3HT nanoparticles, which leads to the same combined layer thicknesses in configurations A and C. Fig. 2 depicts the total absorption of all devices measured in reflection geometry. By multiplying the absorption with the AM1.5 solar photon flux in the relevant absorption regime between 325 nm and 650 nm and calculating the overall number of absorbed photons, we verified that the devices A, B and C indeed do harvest the same number of photons within a maximum deviation of 2%.

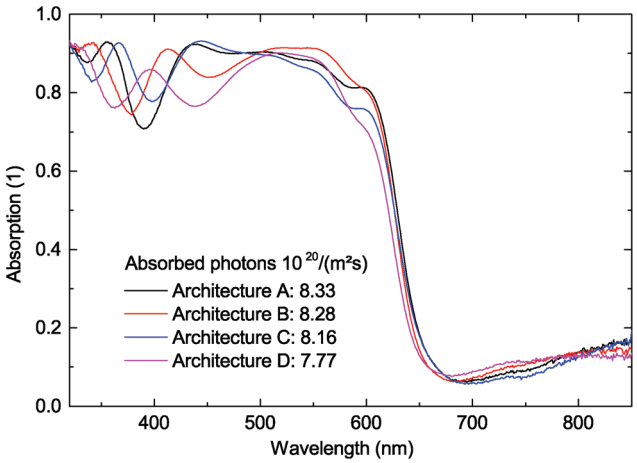

Fig. 2 Absorption spectra calculated from total reflectance measurements of the devices A, B, C and D. The short-wavelength modulations of the spectra originate from thin-film interferences due to different layer thicknesses. The total numbers of absorbed photons were calculated by multiplying the absorption (1 – reflectance) with the AM1.5 photon flux and integration between 325 and 650 nm. By design, all devices show about equal photon harvesting properties.

Vertical material distribution

In order to investigate the vertical material distribution within the photo-active layer, we studied the proxy devices (i) and (ii) depicted in Fig. 3. Sample (i) employs a thermally annealed (150 °C, 10 min) nanoparticulate P3HT:ICBA photo-active layer (150 nm), whereas sample (ii) comprises an additional ther-

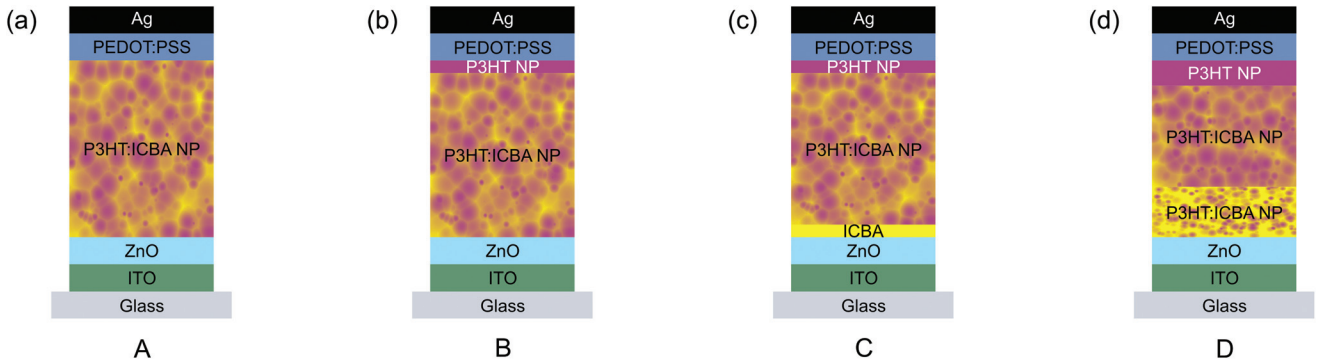

Fig. 1 Device architectures: (a) Reference device comprising a ITO/ZnO bottom cathode and a PEDOT:PSS/Ag top anode as well as a nanoparticulate P3HT:ICBA absorber layer. (b) Neat P3HT nanoparticles were introduced between the absorber layer and the PEDOT:PSS layer. The nanoparticulate P3HT top layer is not closed with its thickness of 15 nm representing the average layer thickness. The thickness of the entire absorber layer was reduced to match the overall amount of P3HT in configuration A. (c) A 15 nm nanoparticulate P3HT and a 20 nm ICBA interlayer were introduced. The overall amount of P3HT and ICBA approximately matches the reference device. (d) The vertical composition of the P3HT:ICBA layer was varied by subsequent deposition of nanoparticles with different mixing ratios (1 : 3, 1 : 1, neat P3HT).

 This journal is © The Royal Society of Chemistry 2016

Open Access Article. Published on 25 February 2016. Downloaded on 1/18/2026 1:16:03 PM.
This article is licensed under a Creative Commons Attribution 3.0 Unported Licence.

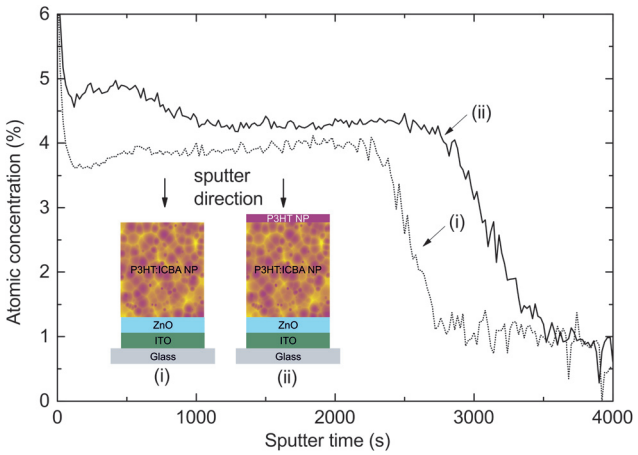

Fig. 3 XPS sputter depth profiles showing the sulfur S 2p signal intensity for C–S groups at 163.5 eV throughout a nanoparticulate P3HT:ICBA layer without (dotted line) and with (solid line) an additional nanoparticulate P3HT top layer. We note that the sputter time cannot be translated directly to the sputter depth due to different ablation speeds for different material compositions.

mally annealed (150 °C, 10 min) neat P3HT layer with a nominal thickness of 15 nm on top, the latter being also deposited from nanoparticle dispersion. We note that the neat P3HT nanoparticles did not form a closed layer which is reflected in the nominal layer thickness being smaller than the nanoparticle size. To mimic the conditions in solar cells, the photo-active layers were deposited atop an ITO/ZnO electrode. However, we omitted the top electrode to have access to the BHJ.

We recorded X-Ray Photoelectron Spectroscopy (XPS) sputter depth profiles of both samples using an Ar^+ ion beam at 3 keV. Fig. 3 shows the sulfur S 2p signal of the C-S groups at 163.5 eV[18] throughout a typical nanoparticulate P3HT:ICBA layer (sample (i), dotted line) and the nanoparticulate P3HT:ICBA/P3HT bilayer (sample (ii), solid line) *versus* sputter time. The decay of the S 2p signal of sample (ii) is shifted to later sputter times, reflecting an overall thicker P3HT:ICBA/P3HT bilayer as compared to the P3HT:ICBA absorber in the reference sample (i). More importantly, we found a significant increase of the S 2p signal intensity on sample (ii) at early sputter times which can be attributed to a P3HT rich top layer as intended by the sequential deposition of P3HT:ICBA and P3HT.

Whereas XPS is a helpful tool to monitor P3HT, it does not readily allow for monitoring fullerenes. It has been observed in earlier publications that fullerenes can migrate within P3HT:fullerene BHJs upon annealing and hence may change the vertical composition of BHJs.[19,20] In order to probe the nominally fullerene-free P3HT top layer for ICBA molecules, that may have diffused from the P3HT:ICBA layer below, we performed Kelvin Probe Force Microscopy (KPFM) imaging on a typical proxy sample (ii) (see Fig. 3 inset) before and after sample annealing (150 °C, 10 min). Fig. 4a and b show the respective film topography and the contact potential difference (CPD)

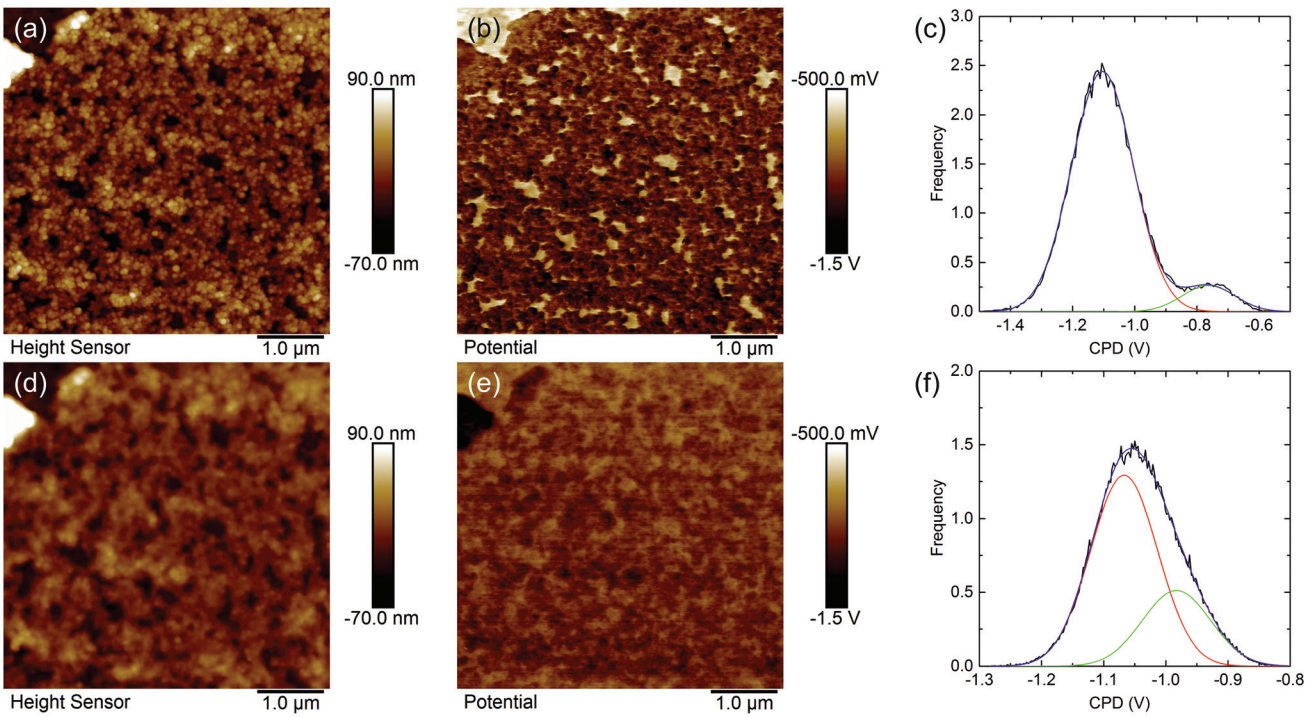

Fig. 4 (a) 5 μm × 5 μm topography and (b) KPFM image of P3HT nanoparticles applied atop P3HT:ICBA nanoparticles directly after deposition. (c) CPD histogram generated from (b). (d) Topography and (e) KPFM image of the same sample after annealing at 150 °C for 10 min. The contrast between the P3HT nanoparticles and the underlying P3HT:ICBA layer is significantly reduced. (f) CPD histogram generated from (e).

Open Access Article. Published on 25 February 2016. Downloaded on 1/18/2026 1:16:03 PM.
This article is licensed under a Creative Commons Attribution 3.0 Unported Licence.

between the Pt/Ir coated KPFM tip and the as-deposited P3HT nanoparticles atop a thermally annealed (150 °C, 10 min) nanoparticulate P3HT:ICBA BHJ, respectively. In both images, P3HT nanoparticles are clearly visible exhibiting a surface roughness R_q = 18 nm and an average ΔCPD = 340 ± 90 mV between the P3HT nanoparticles and the nanoparticulate P3HT:ICBA surface below. ΔCPD was calculated from the distance of the two main peaks in the KPFM image histogram in Fig. 4c. The high ΔCPD allows to distinguish between the P3HT nanoparticles and the underlying P3HT:ICBA layer, the latter having a higher work-function (bright areas in Fig. 4b). We note that the topography can cross-talk to the KPFM signal. However, for P3HT nanoparticles on plain P3HT we measured a ΔCPD of about 30 ± 60 mV only (data not shown here), which is much lower than the ΔCPDs measured between the P3HT nanoparticles and the nanoparticulate P3HT:ICBA surface. Hence, cross-talk from the topography signal to the KPFM signal cannot explain the high ΔCPD observed here.

As depicted in Fig. 4d and e, thermal annealing after P3HT nanoparticle deposition leads to smearing out of both the topography and the CPD signal due to deformation of the nanoparticles and flattening of the layer by filling the voids, the latter being reflected in the somewhat lower surface roughness R_q = 13 nm. Most importantly, the ΔCPD between the P3HT nanoparticles and the nanoparticulate P3HT:ICBA surface significantly drops to 85 ± 55 mV, with the two main peaks of the histogram merging (Fig. 4f). We attribute this ΔCPD drop to ICBA diffusion from the underlying nanoparticulate P3HT:ICBA layer into the nanoparticulate P3HT top layer as it was observed for P3HT:fullerene BHJs upon annealing in earlier publications for layers deposited from solution.[19,20] However, with the average ΔCPD of the annealed sample being larger than the typical topography cross-talk, we conclude that the top layer after annealing is still P3HT rich.

Taking into account the change of ΔCPD upon annealing and the sulfur XPS sputter depth profiles of the proxy devices, we conclude converse vertical polymer and fullerene gradients within the photo-active layers of type B and C solar cells, with a P3HT rich top layer.

Optoelectronic device properties

After probing the vertical material distribution in multi-layer architectures deposited from nanoparticle dispersions, we investigated its impact on the optoelectronic properties of photovoltaic devices. The current density–voltage (J–V) curves of the solar cells are depicted in Fig. 5. Their key performance data – open circuit voltage (V_{oc}), short-circuit current density (J_{sc}), fill factor (FF) and the PCE are summarized in Table 1.

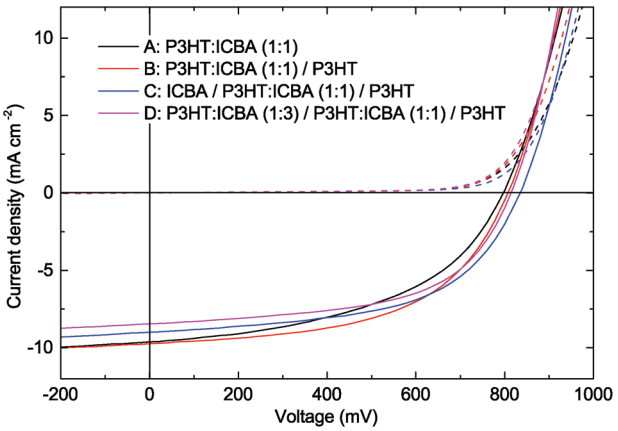

Fig. 5 J–V curves of the nanoparticulate solar cells with and without additional nanoparticulate P3HT or ICBA layers. The introduction of a vertically graded material distribution leads to an enhanced open-circuit voltage (V_{oc}) and fill factor (FF).

Configuration A reference devices exhibit J_{sc} = 9.6 mA cm^{-2}, V_{oc} = 797 mV, FF = 48%, altogether yielding a PCE = 3.7%. We note that any deviations of the processing parameters (see the Methods section) or the key performance parameters from earlier reports may originate from batch-to-batch variations of P3HT. Upon introducing P3HT nanoparticles below the anode (configuration B), V_{oc} improves slightly to 808 mV whereas J_{sc} remains unchanged. The PCE improves to 4.2% which reflects the better FF = 53%. An additional ICBA interlayer in configuration C further enhances the V_{oc} to 834 mV. The improvement of the V_{oc} in comparison with the reference device A may indicate a reduced charge carrier recombination, due to the blocking of opposite charges by the interlayers at the electrodes.[21] In general, the fill factor reflects the field dependence of the photo current density, which is ruled by charge carrier recombination and extraction.[22] In order to study the charge carrier recombination processes in devices A, B and C, we performed light-intensity dependent photocurrent measurements, utilizing neutral density (ND) filters between the solar simulator and the samples. As depicted in Fig. 6a, for all three device configurations A, B and C, we find a similar $J_{sc} \sim I^{\alpha}$ ($\alpha \approx 0.95$) dependence of the short-circuit current density on the illumination intensity I. With α being close to unity, we conclude predominant monomolecular

Table 1 Key performance parameters of the nanoparticulate solar cells, averaged over at least 8 devices. h represents the active layer thickness including the thickness of the neat ICBA or nanoparticulate P3HT layers

Absorber layer configuration	h (nm)	J_{sc} (mA cm^{-2})	V_{oc} (mV)	FF (%)	PCE (%)
A: P3HT:ICBA	196 ± 4	9.6 ± 0.1	797 ± 1	48 ± 1	3.7 ± 0.1
B: P3HT:ICBA/P3HT	174 ± 3	9.8 ± 0.1	808 ± 2	53 ± 1	4.2 ± 0.1
C: ICBA/P3HT:ICBA/P3HT	200 ± 4	9.0 ± 0.1	834 ± 2	55 ± 1	4.2 ± 0.1
D: P3HT:ICBA (1 : 3)/P3HT:ICBA (1 : 1)/P3HT	149 ± 12	8.5 ± 0.1	814 ± 5	56 ± 1	3.9 ± 0.1

This journal is © The Royal Society of Chemistry 2016

Open Access Article. Published on 25 February 2016. Downloaded on 1/18/2026 1:16:03 PM.
This article is licensed under a Creative Commons Attribution 3.0 Unported Licence.

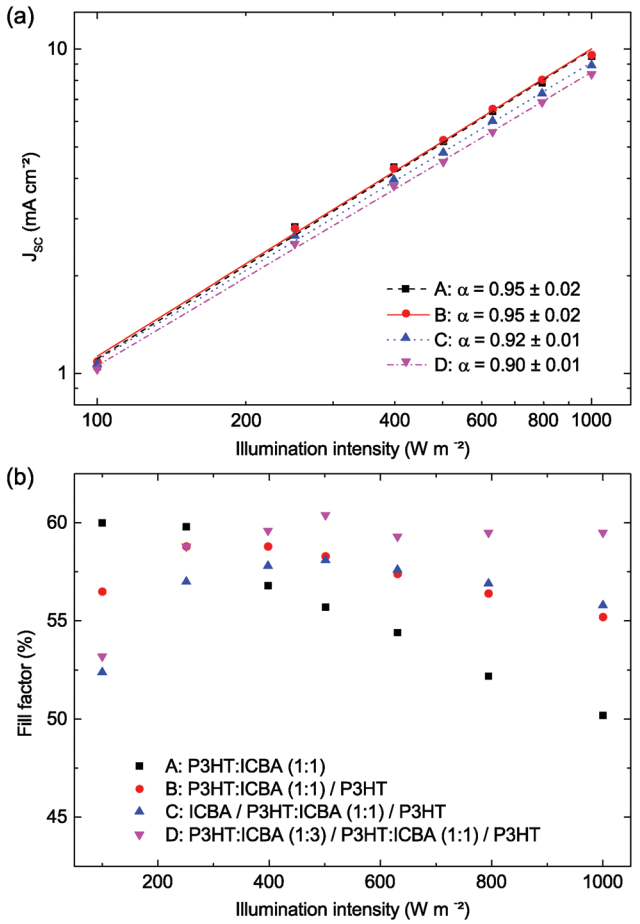

Fig. 6 Illumination dependent measurements of (a) the short circuit current density (J_{sc}) and (b) the fill factor (FF). J_{sc} *vs.* illumination intensity yields similar α for all architectures, whereas the FF decrease is less pronounced for graded absorber layers under higher illumination intensities. For reasons of clarity, we show the data of one typical device out of four, thereby accepting minor differences to the average data in Table 1 under one sun illumination.

recombination, negligible bimolecular recombination and hence good extraction of free charge carriers at a high internal field in devices A–C, being well in accordance with the properties of BHJs processed from a blend solution.[23] When moving to lower internal fields, *e.g.*, at the maximum power point (MPP), the influence of bimolecular recombination increases. Accordingly, we attribute the higher FFs and the higher current densities at MPP (J_{MPP}) of configuration B and C devices to lower bimolecular recombination losses at a low internal field and thus to improved charge carrier extraction *via* enhanced percolation pathways: due to the P3HT-rich layer below the anode, hole percolation to the anode is improved. Likewise, the ICBA layer improves electron percolation to the cathode. At the same time, the extraction of oppositely charged carriers is suppressed.

Further insight into the origin of the FF can be gained from the dependence of the FF on the illumination intensity in Fig. 6b. At an illumination intensity I = 400 W m^{-2}, all devices show a similar FF. Towards higher illumination intensities, and hence towards higher concentrations of (photo-generated) charge carriers, the FF drops due to the increased bimolecular recombination, with the effect being less pronounced for the configurations B and C that feature P3HT or P3HT and ICBA layers. Due to the improved charge carrier extraction in devices B and C, the influence of an increase in bimolecular recombination is lower, leading to a less significant drop of the FF at higher illumination intensities. At very low illumination intensities, the FF drops as known from calculations using the modified equivalent circuit model.[24]

Graded polymer/fullerene mixing ratios

P3HT gradients and converse ICBA gradients can also be introduced by synthesizing and depositing P3HT:ICBA nanoparticles with different mixing ratios. Therefore, we sequentially applied P3HT:ICBA (1 : 3) nanoparticles, P3HT:ICBA (1 : 1) nanoparticles and neat P3HT nanoparticles atop the ITO/ZnO cathode according to the device architecture D depicted in Fig. 1.

The corresponding *J–V* curve is depicted in Fig. 5 and the key performance parameters are summarized in Table 1. Again, we observed an enhanced V_{oc} = 814 mV and FF = 56% *versus* the reference device configuration A. The J_{sc} = 8.5 mA cm^{-2} is reduced by about 11% in configuration D which we attribute to the lower total thickness h = 149 nm of the photo-active layer, being well in accordance with about 7% reduced total device absorption (Fig. 2). Still, the PCE yields 3.9% thereby outperforming device A. In the light-intensity dependent J_{sc} measurements in Fig. 6a, we find α = 0.9 which is close to configurations A–C indicating similar recombination processes within the active layer under J_{sc} conditions. As the graded absorber structure provides optimized charge carrier percolation *via* increasing domain sizes to the respective electrodes, the blocking effect of oppositely charged carriers towards the wrong electrode is optimal. Accordingly, we did not observe any significant dependence of the FF *versus* the illumination intensity between I = 250 W m^{-2} and I = 1000 W m^{-2} (Fig. 6b).

Conclusions

Besides eco-friendly processing, organic BHJ nanoparticle dispersions allow the fabrication of multi-layers and, in particular, graded photo-active layers in organic solar cells. The latter device architecture provides enhanced percolation paths for photo-generated charge carriers to the respective electrodes as concluded from the recombination regimes investigated by illumination intensity dependent photocurrent and fill factor measurements. In contrast to state-of-the-art solution processing, these multi-layer architectures become feasible due to the unique processing properties of polymer:fullerene nanoparticles, not being soluble in processing agents after layer deposition. With the concept of multi-layer deposition from organic nanoparticle dispersions being readily transferable to

Open Access Article. Published on 25 February 2016. Downloaded on 1/18/2026 1:16:03 PM.
This article is licensed under a Creative Commons Attribution 3.0 Unported Licence.

other device architectures and other organic optoelectronic devices, it may well be a versatile tool for future eco-friendly printing of advanced organic optoelectronic devices.

Methods

Nanoparticle synthesis

Organic nanoparticles were precipitated from poly(3-hexylthiophene-2,5-diyl) (P3HT, Rieke Metals, M_W = 57 000 g mol^{-1}, $Đ_M$ = 2.4, RR = 91%) and indene-C_{60} bisadduct (ICBA, Lumtec) solution without using surfactants.[12] Therefore, neat P3HT or mixtures of P3HT and ICBA were dissolved in chloroform ($CHCl_3$) in different weight ratios (1 : 0.8, 1 : 1 and 1 : 3 w/w). The solutions were added constantly to the non-solvent ethanol (EtOH) under vigorous stirring. After precipitation, $CHCl_3$ was evaporated without stirring. Then the non-solvent phase was reduced to yield particle concentrations of 2.5–10 mg mL^{-1} and particle sizes of 80–110 nm as determined by dynamic light scattering (DLS).

Device fabrication

Organic solar cells were fabricated according to the device architecture depicted in Fig. 1 on patterned, indium tin oxide (ITO) coated glass substrates that were cleaned by subsequent ultrasonication in acetone and isopropanol (10 min) before exposing them to an oxygen plasma in order to remove organic residues from the ITO surface (2 min). All subsequent device fabrication steps were carried out under a N_2 atmosphere. A zinc oxide (ZnO) nanoparticle dispersion (Nanograde Ltd, N-10, 2.5 wt% in isopropanol) was diluted with isopropanol to yield a concentration of 1 wt%, spin cast (4000 rpm, 30 s, 20 nm) and then thermally annealed (150 °C, 10 min). The active layer was deposited by iterative spin coating of different nanoparticle dispersions on a rotating substrate (1000 rpm). For reference devices, configuration A, P3HT:ICBA (1 : 1) was spin cast four times from dispersion (3 × 10 mg mL^{-1}, 1 × 5 mg mL^{-1}). For configuration B, a P3HT:ICBA dispersion (1 : 1, 10 mg mL^{-1}) was spin cast three times followed by a neat P3HT dispersion (2.5 mg mL^{-1}). For configuration C, ICBA was spin cast from 1,2-dichlorobenzene (20 mg mL^{-1}, 2000 rpm, 30 s, 20 nm) and thermally annealed (80 °C, 5 min) before depositing the layer sequence used for configuration B. The active layer of configuration D was deposited by spin coating a P3HT:ICBA dispersion (1 : 3, 5 mg mL^{-1}) twice, a P3HT:ICBA dispersion (1 : 1, 10 mg mL^{-1}) twice and a neat P3HT dispersion (5 mg mL^{-1}) once. The samples were annealed on a hotplate (150 °C, 10 min). Poly(3,4-ethylenedioxythiophene):polystyrene sulfonate (PEDOT:PSS, HTL Solar, Heraeus) was water-diluted (1 : 1 v/v) and then spin coated (500 rpm, 5 s; 2000 rpm, 30 s; 35 nm) on top. The samples were annealed on a hotplate (120 °C, 10 min). The silver (Ag, *ca.* 100 nm) top electrode was thermally evaporated (10^{-6} mbar) using a shadow mask to define the active area of the solar cells (3 × 3.5 mm^2).

For Atomic Force Microscopy (AFM), Kelvin Probe Force Microscopy (KPFM) and X-Ray Photoelectron Spectroscopy (XPS) sputter depth profile measurements, proxy devices were fabricated on glass substrates coated with unpatterned ITO, that were cleaned by subsequent ultrasonication in acetone and isopropanol before (10 min). ZnO was deposited as described above. The P3HT:ICBA dispersion (1 : 0.8, 5 mg mL^{-1}) was spin cast six times, and the samples were annealed on a hotplate (150 °C, 10 min) before a neat P3HT dispersion (5 mg mL^{-1}) was spin cast atop. KPFM measurements were performed before and after annealing (150 °C, 10 min). XPS sputter depth profiles were recorded on this sample (sample (ii) in Fig. 3) and on a reference sample (sample (i) in Fig. 3), the latter exhibiting only the P3HT:ICBA layer (1 : 0.8, 5 mg mL^{-1} dispersion, spin cast six times).

Characterization

UV/Vis reflectance spectra of all devices (configurations A–D) were recorded at room temperature with an Agilent Cary 5000 spectrophotometer equipped with a 150 mm diameter integrating sphere.

AFM and single-pass FM-KPFM (Frequency Modulation) images were recorded in tapping mode on a Bruker Dimension ICON utilizing an Ir/Pt coated FMV-PT tip, with the contact potential difference CPD = $\Phi_{tip} - \Phi_{sample}$ and $\Phi < 0$.

XPS measurements were performed using a K-Alpha+ XPS instrument (Thermo Fisher Scientific, East Grinstead, UK). Data acquisition and processing using the Thermo Avantage software is described elsewhere.[25] All samples were analyzed using a microfocused, monochromated Al Kα X-ray source (30–400 μm spot size). The analyzer transmission function, Scofield sensitivity factors,[26] and effective attenuation lengths (EALs) for photoelectrons were applied for quantification. EALs were calculated using the standard TPP-2M formalism.[27] All spectra were referenced to the C1s peak of hydrocarbon at 285.0 eV binding energy, controlled by means of the well-known photoelectron peaks of metallic Cu, Ag, and Au. Sputter depth profiles were performed using a raster scanned Ar^+ ion beam (2 × 4 mm^2) at 3 keV and 30° angle of incidence.

Current density–voltage (J–V) curves were recorded with a Keithley 238 source-meter under illumination by using a spectrally monitored Oriel solar simulator (300 W, 1000 W m^{-2}, AM 1.5). The sample edges were masked to avoid an overestimation of the photo-current by light-incoupling from the sample edges. For the intensity dependent measurements, a set of 6 neutral density filters (ND 0.1, 0.2, 0.3, 0.4, 0.6 and 1.0) was used.

Acknowledgements

The authors acknowledge fruitful discussions with Ardalan Armin (The University of Queensland) and Christian Sprau (KIT) as well as funding from the Federal Ministry for Education and Research (BMBF), Germany, under contract no 12N12295 (project UNICORN). This work received further financial support from the Gips-Schüle Research Prize 2015. The AFM was made available through funding by the BMBF

 This journal is © The Royal Society of Chemistry 2016

under contract no 03EK3504 (project TAURUS). The authors thank the DFG Center for Functional Nanostructures (CFN) for support. C. Feldmann and L. Brütsch (Institute of Inorganic Chemistry, KIT) kindly provided the DLS measurement setup. ZnO nanoparticles were provided by Nanograde Ltd. The XPS instrument was supported by the Federal Ministry of Economics and Technology on the basis of a decision by the German Bundestag.

Open Access Article. Published on 25 February 2016. Downloaded on 1/18/2026 1:16:03 PM.
This article is licensed under a Creative Commons Attribution 3.0 Unported Licence.

References

1 A. J. Moulé, *Curr. Opin. Solid State Mater. Sci.*, 2010, **14**, 123.
2 R. Søndergaard, M. Hösel, D. Angmo, T. T. Larsen-Olsen and F. C. Krebs, *Mater. Today*, 2012, **15**, 36.
3 R. Po, A. Bernardi, A. Calabrese, C. Carbonera, G. Corso and A. Pellegrino, *Energy Environ. Sci.*, 2014, **7**, 925.
4 C. Sprau, F. Buss, M. Wagner, D. Landerer, M. Koppitz, A. Schulz, D. Bahro, W. Schabel, P. Scharfer and A. Colsmann, *Energy Environ. Sci.*, 2015, **8**, 2744.
5 G. Susanna, L. Salamandra, C. Ciceroni, F. Mura, T. M. Brown, A. Reale, M. Rossi, A. Di Carlo and F. Brunetti, *Sol. Energy Mater. Sol. Cells*, 2015, **134**, 194.
6 C.-C. Chueh, K. Yao, H.-L. Yip, C.-Y. Chang, Y.-X. Xu, K.-S. Chen, C.-Z. Li, P. Liu, F. Huang, Y. Chen, W.-C. Chen and A. K.-Y. Jen, *Energy Environ. Sci.*, 2013, **6**, 3241.
7 O. Synooka, K.-R. Eberhardt and H. Hoppe, *RSC Adv.*, 2014, **4**, 16681.
8 T. R. Andersen, T. T. Larsen-Olsen, B. Andreasen, A. P. L. Böttiger, J. E. Carlé, M. Helgesen, E. Bundgaard, K. Norrman, J. W. Andreasen, M. Jørgensen and F. C. Krebs, *ACS Nano*, 2011, **5**, 4188.
9 S. Ulum, N. Holmes, M. Barr, A. L. D. Kilcoyne, B. Bin Gong, X. Zhou, W. Belcher and P. Dastoor, *Nano Energy*, 2013, **2**, 897.
10 T. S. Gehan, M. Bag, L. A. Renna, X. Shen, D. D. Algaier, P. M. Lahti, T. P. Russell and D. Venkataraman, *Nano Lett.*, 2014, **14**, 5238.
11 K. Landfester, R. Montenegro, U. Scherf, R. Güntner, U. Asawapirom, S. Patil, D. Neher and T. Kietzke, *Adv. Mater.*, 2002, **14**, 651.
12 S. Gärtner, M. Christmann, S. Sankaran, H. Röhm, E.-M. Prinz, F. Penth, A. Pütz, A. E. Türeli, B. Penth, B. Baumstümmler and A. Colsmann, *Adv. Mater.*, 2014, **26**, 6653.
13 S. Sankaran, K. Glaser, S. Gärtner, T. Rödlmeier, K. Sudau, G. Hernandez-Sosa and A. Colsmann, *Org. Electron.*, 2016, **28**, 118.
14 S. Heutz, P. Sullivan, B. M. Sanderson, S. M. Schultes and T. S. Jones, *Sol. Energy Mater. Sol. Cells*, 2004, **83**, 229.
15 L. Chen, Y. Tang, X. Fan, C. Zhang, Z. Chu, D. Wang and D. Zou, *Org. Electron.*, 2009, **10**, 724.
16 H.-L. Huang, C.-T. Lee and H.-Y. Lee, *Org. Electron.*, 2015, **21**, 126.
17 Z. Xu, L.-M. Chen, G. Yang, C.-H. Huang, J. Hou, Y. Wu, G. Li, C.-S. Hsu and Y. Yang, *Adv. Funct. Mater.*, 2009, **19**, 1227.
18 N. Zydziak, C. Hübner, M. Bruns, A. P. Vogt and C. Barner-Kowollik, *Polym. Chem.*, 2013, **4**, 1525.
19 L. N. S. A. Thummalakunta, C. H. Yong, K. Ananthanarayanan and J. Luther, *Org. Electron.*, 2012, **13**, 2008.
20 K. H. Lee, P. E. Schwenn, A. R. G. Smith, H. Cavaye, P. E. Shaw, M. James, K. B. Krueger, I. R. Gentle, P. Meredith and P. L. Burn, *Adv. Mater.*, 2010, **23**, 766.
21 N. Li, B. E. Lassiter, R. R. Lunt, G. Wie and S. R. Forrest, *Appl. Phys. Lett.*, 2009, **94**, 023307.
22 D. Bartesaghi, I. del, C. Pérez, J. Kniepert, S. Roland, M. Turbiez, D. Neher and L. J. A. Koster, *Nat. Commun.*, 2015, **6**, 7083.
23 L. Liu and G. Li, *Sol. Energy Mater. Sol. Cells*, 2011, **95**, 2557.
24 S. Yoo, B. Domercq and B. Kippelen, *J. Appl. Phys.*, 2005, **97**, 103706.
25 K. L. Parry, A. G. Shard, R. D. Short, R. G. White, J. D. Whittle and A. Wright, *Surf. Interface Anal.*, 2006, **38**, 1497.
26 J. H. Scofield, *J. Electron Spectrosc. Relat. Phenom.*, 1976, **8**, 129.
27 S. Tanuma, C. J. Powell and D. R. Penn, *Surf. Interface Anal.*, 1994, **21**, 165.